Heliyon 9 (2023) e16890

Contents lists available at ScienceDirect

Heliyon

journal homepage: www.cell.com/heliyon

Unveiling the effect of shapes and electrolytes on the electrocatalytic ethanol oxidation activity of self-standing Pd nanostructures

Adewale K. Ipadeola [a,b,1], Belal Salah [a,b,1], Alaa Ghanem [c], Doniyorbek Ahmadaliev [d], Mohammed A. Sharaf [e,f], Aboubakr M. Abdullah [a,**], Kamel Eid [b,*]

[a] Center for Advanced Materials, Qatar University, Doha, 2713, Qatar
[b] Gas Processing Center (GPC), College of Engineering, Qatar University, Doha, 2713, Qatar
[c] PVT-Lab, Production Department, Egyptian Petroleum Research Institute, Nasr City, 11727, Cairo, Egypt
[d] Department of Chemical & Material Science Engineering of School of Engineering, New Uzbekistan University, Tashkent, 100007, Uzbekistan
[e] Department of Maritime Transportation Management Engineering, Istanbul University-Cerrahpasa, 34320, Avcilar/Istanbul, Turkey
[f] Mericler Inc. Educational Consulting, Esentepe, Yazarlar Sk. No 21, 34381, Sisli/Istanbul, Turkey

ARTICLE INFO

Keywords:
Pd nanocrystals
Pd clustered nanospheres
Pd nanocubes
Ethanol oxidation
The effect of shapes
The effect of electrolytes

ABSTRACT

Morphologically controlled Pd-based nanocrystals are the most efficient strategies for improving the electrocatalytic ethanol oxidation reaction (EOR) performance; however, their morphological-EOR activity relationship and effect of electrolytes at a wide pH range are still ambiguous. Here, we have synthesized porous self-standing Pd clustered nanospheres (Pd-CNSs) and Pd nanocubes (Pd-NCBs) for the EOR in acidic (H_2SO_4), alkaline (KOH), and neutral ($NaHCO_3$) electrolytes compared to commercial spherical-like Pd/C catalysts. The fabrication process comprises the ice-cooling reduction of Pd precursor by sodium borohydride ($NaBH_4$) and L-ascorbic acid to form Pd-CNSs and Pd-NCBs, respectively. The EOR activity of Pd-CNSs significantly outperformed those of Pd-NCBs, and Pd/C in all electrolytes, but the EOR activity was better in KOH than in H_2SO_4 and $NaHCO_3$. This is due to the 3D porous clustered nanospherical morphology that makes Pd active centers more accessible and maximizes their utilization during EOR. The EOR specific/mass activities of Pd-CNSs reached (8.51 mA/cm^2/2.39 A/mg$_{Pd}$) in KOH, (2.98 mA/cm^2/0.88 A/mg$_{Pd}$) in H_2SO_4, and (0.061 mA/cm^2/0.0083 A/mg$_{Pd}$) in $NaHCO_3$, in addition to stability after 1000 cycles. This study affirms that porous 3D spherical Pd nanostructures are preferred for the EOR than those of 0D spherical-like and multi-dimensional cube-like nanostructures.

1. Introduction

The pursuit of developing environmentally benign and sustainable energy systems arose an enormous interest in fuel cell

* Corresponding author.
** Corresponding author.
E-mail addresses: bakr@qu.edu.qa (A.M. Abdullah), kamel.eid@qu.edu.qa (K. Eid).
[1] Equal contribution.

https://doi.org/10.1016/j.heliyon.2023.e16890
Received 3 March 2023; Received in revised form 26 May 2023; Accepted 31 May 2023
Available online 2 June 2023

technologies, amongst which employed alcohol (i.e., methanol, glucose, and ethanol) [1,2], oxygen [3], solar-cells [4], biofuel [5], and hydrogen [6–8]. Ethanol-based fuel cell (EFC) is a promising energy device that converts chemical energy from ethanol fuel into electricity because of its low toxicity and low cost, high energy density, efficiency and negligible greenhouse gas emission [9–13]. Despite the great potential of the EFC, its anodic reaction (i.e., ethanol oxidation reaction (EOR)) and sluggish kinetics of oxygen reduction reaction (ORR) at the cathode side of the EFC are the major determinants for the optimum functioning of the fuel cell. Hence, necessitates the utilization of excellent electrocatalysts [14–17]. Palladium (Pd) nanocrystals are excellent materials for EOR electrocatalysis and are extremely tolerant to carbonaceous species poisoning, particularly in alkaline media [18–24]. Studies are most concerned with the enhancement of the Pd nanocrystals' electrocatalytic EOR performance and stability [25,26].

Tailoring the morphology of Pd nanocrystals is a crucial strategy adopted for boosting the nanocatalysts' physicochemical merits for favorable EOR electrocatalysis and stability than the conventional catalysts (i.e., Pd/C) [13,27–32]. Different Pd nanocrystals with unique morphologies, such as spherical nanoparticles, multi-twinned particles, spherical, single-crystalline nanoflowers, nanocubes, urchin-like nanoparticles, concave tetrahedral, tetrapods and nanosheets were rationally designed and fabricated with impressive liquid fuels electrocatalysis, due to their porous and interconnected structure, high surface area and abundant absorption sites, besides their great tolerance to carbonaceous or intermediate species [33–35]. For example, chestnut-bur-like Pd nanostructures exhibited superior EOR mass activity (0.57 A/mg_{Pd}) to Pd nanocube (0.32 A/mg_{Pd}), Pd nano-octahedron (0.22 A/mg_{Pd}) and Pd/C (0.38 A/mg_{Pd}) by factors of 1.78, 2.59 and 1.5, respectively, owing to the large surface area and rich catalytic active sites of the chestnut-bur-like structures [36]. The EOR electrocatalysis of Pd trigonal bipyramidal/tetrahedral nanocrystals on Vulcan carbon (Pd TBTs/C, 1.59 A/mg_{Pd}) was 1.59 times higher than Pd/C (0.96 A/mg_{Pd}), besides its improved stability after 5000 s, attributable to the unique shape with vertexes, edges, facets and coordinated atoms [37]. Size-controlled multipod Pd nanostructures (PdMNPs (Pd30)) displayed increased EOR specific/mass activity (6.56 mA/cm^2/1.42 A/mg_{Pd}) by 2.34/2.96 times to spherical Pd nanoparticles (PdSNPs (Pd10)), due to the high surface energy and surface area of the multipod structures [38]. Indeed, the importance of the structures and sizes of Pd nanocrystals cannot be overemphasized for EOR electrocatalysis. Various synthesis methods, like template-assisted [39], polyol [40], solvothermal/hydrothermal [41], galvanic replacement [42], laser ablation [43], seed-mediated [44] and aqueous solution reduction [45], employed for the synthesis of distinct structures of Pd electrocatalysts, are either tedious or complicated. However, the controlled high-mass production of Pd-based catalysts for EOR remains a grand challenge [46–48]. Also, the morphological-EOR activity relationship of self-standing Pd nanostructures and the effect of electrolytes at a wide pH range are not yet reported.

In this regard, porous self-standing Pd clustered nanospheres (Pd-CNSs) and Pd nanocubes (Pd-NCBs) were synthesized for the electrocatalytic EOR and benchmarked to the commercial spherical-like Pd/C catalysts. The nanocatalysts' formation process comprises the chemical reduction of potassium tetrachloropalladate(II) (K_2PdCl_4) by sodium borohydride ($NaBH_4$) at 0 °C to produce Pd-CNSs and by ascorbic acid to form Pd-NCBs. The EOR activity and stability of 3D porous Pd-CNSs, Pd-NCBs, and Pd/C nanostructures were tested in alkaline KOH (pH = 12), acidic H_2SO_4 (pH = 2) and neutral $NaHCO_3$ (pH = 7.4) at room temperature to investigate the effect of catalysts' shapes and electrolytes.

2. Experimental

2.1. Materials/chemicals

Potassium tetrachloropalladate (II) (K_2PdCl_4, ≥ 99 %), sodium borohydride ($NaBH_4$, 99 %), polyvinylpyrrolidone (PVP), L-ascorbic acid (AA, ≥ 99%), potassium hydroxide (KOH, ≥ 85 %), sulfuric acid (H_2SO_4, 95–98 %), sodium hydrogencarbonate ($NaHCO_3$, ≥ 95 %), commercial Pd/C (10 wt. %) were purchased from Sigma-Aldrich Chemie GmbH (Munich Germany).

2.2. Preparation of Pd-CNSs

The Pd-CNSs nanocrystals were prepared based on the previously reported method [49], but with slight modifications, including the drop-wise addition of an aqueous solution of $NaBH_4$ (0.1 M, 1.0 mL) to an aqueous solution of K_2PdCl_4 (15 mM, 10 mL) in an ice bath at 0 °C under sonication for 2 min. The obtained opaque black precipitate of Pd-CNSs was dispersed in deionized water, centrifuged at 7000 rpm for 5 min, washed with water severally, dried, and then stored for further use.

2.3. Preparation of Pd-NCBs

The Pd-NCBs nanocrystals were synthesized based on previously reported method [50], but with slight changes, including the initial mixing of an aqueous solution of K_2PdCl_4 (15 mM, 10 mL) with PVP (13.0 mg) under sonication for 30 s, then quick addition of L-ascorbic acid (0.1 M, 1.0 mL) under sonication for 20 min. The obtained opaque black precipitate of Pd-CNBs was centrifuged at 7000 rpm for 5 min and washed severally with deionized water to remove PVP residues, then dried and kept for further use.

2.4. Materials characterization

A scanning electron microscope ((SEM), Hitachi S-4800, Hitachi, Tokyo, Japan) equipped with Energy Dispersive X-Ray Analyzer (EDX) and a transmission electron microscope ((TEM), TecnaiG220, FEI, Hillsboro, OR, USA) were used for imaging and composition analysis. The X-ray photoelectron spectroscopy ((XPS) was carried out on (Ultra DLD XPS Kratos, Manchester, UK). The X-ray diffraction (XRD) was conducted on (X'Pert-Pro MPD, PANalytical Co., Almelo, Netherlands). The inductively coupled plasma optical

emission spectrometry ((ICP-OES) was performed on (ICP-OES, Agilent 5800, USA).

2.5. Ethanol oxidation reaction (EOR) measurements

The electrochemical EOR measurements were conducted on Gamry potentiostat (Reference 3000, Gamry Co., Warminster, PA, USA) using the three-electrode configuration, comprising Pt wire, Ag/AgCl, and glassy carbon (GC, 5 mm), as counter, reference and working electrodes, respectively. A 2.0 mg of each electrocatalyst (as-prepared without any support) was dispersed in an aqueous solution of isopropanol/H_2O/Nafion (0.05 wt. %) (3/1/1 v/v/v ratio) and drop cast onto the cleaned GC electrodes, and the electrodes were left to dry in an oven under vacuum at 80 °C for 1 h. The mass loading of Pd in the electrocatalysts modified on the GCE was approximately 0.2831 ± 0.0001 μg_{Pd}, as determined by the ICP-OES. Electrochemical CO stripping of the Pd nanocrystals and Pd/C was carried out in CO saturated 1.0 M KOH for 30 min, using cyclic voltammetry (CV) at potential window (−0.1 to 1.2 V *vs.* RHE) and 50 mV/s, then the CO gas was switched to N_2 and purged for 30 min, then the CV scan repeated. The electrochemical active surface area (ECSA) was calculated from ECSA $= \frac{Q}{S \times l}$, where Q, S and l are the coulombic charge of the integrated PdO peak, coulombic

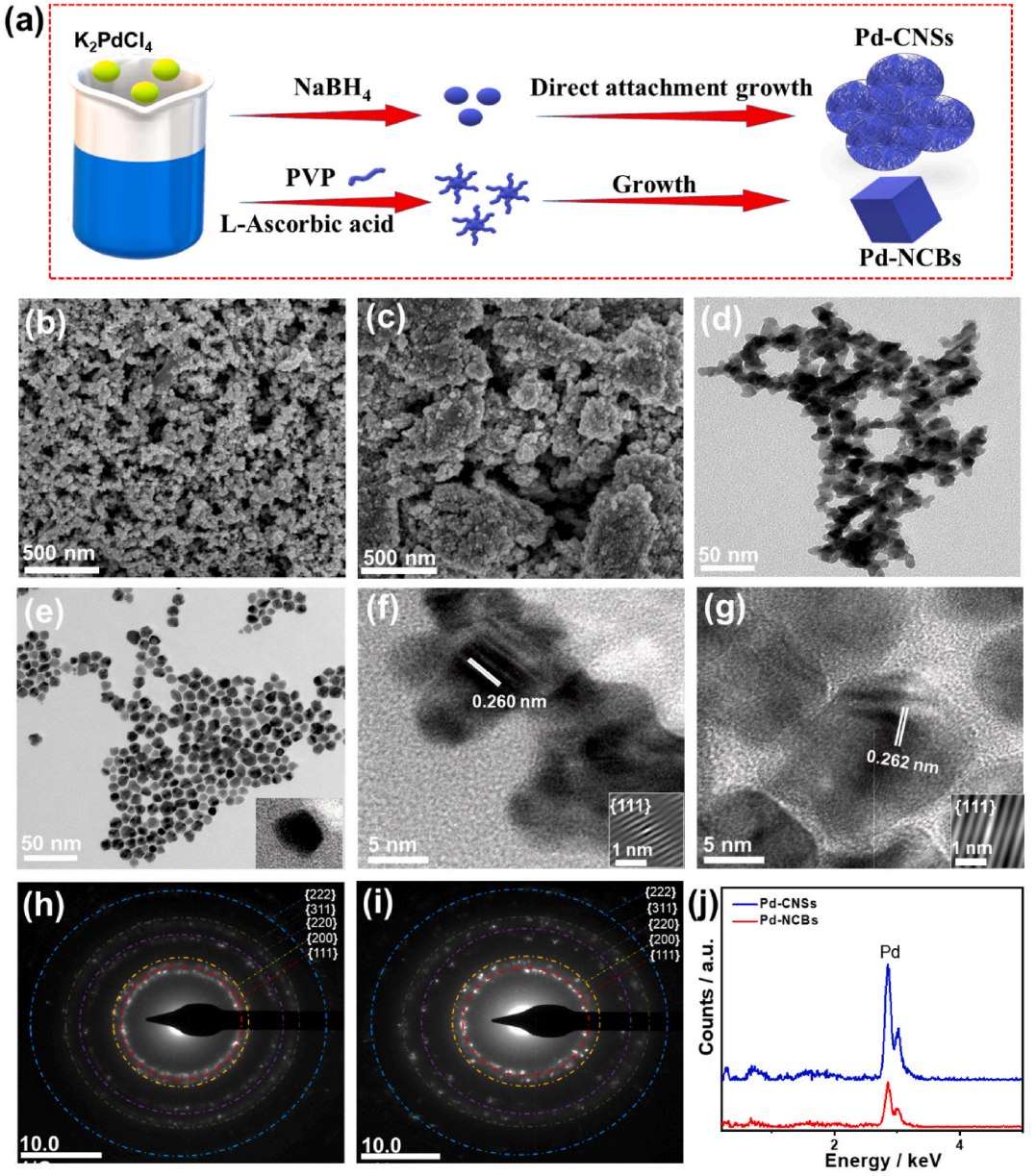

Fig. 1. The aqueous-solution reduction synthetic scheme (a), SEM images (b, c), TEM images (d, e), HRTEM images (f, g), SAED (h, i) and EDX analysis (j) of Pd-CNSs and Pd-NCBs, respectively.

constant for monolayer Pd (0.424 mC cm^{-2}) and mass loading of Pd.

3. Results and discussion

Fig. 1a shows the synthetic schemes for the preparation of the Pd-CNSs and Pd-NCBs, which involve the direct chemical reduction of K_2PdCl_4 at 0 °C by $NaBH_4$ and L-ascorbic acid, respectively. The $NaBH_4$ with its severe reduction power induces the burst nucleation of Pd^{2+} to form multiple Pd nuclei which are highly energetic and coalescence to reduce their total surface energies, resulting in direct attachment growth to yield porous Pd clustered nanospheres (Pd-CNSs). Meanwhile, the sluggish reduction of ascorbic acid promotes the reduction of Pd^{2+} to produce Pd nuclei, covered by the adsorption of PVP on Pd nuclei and acts as a structure-directing agent leading to homogenous growth to form porous Pd cubic-like nanostructure (Pd-NCBs). This is evident in the SEM images, which display the formation of Pd-CNSs in 3D porous clustered spheres composed of ultra-small nanoparticles (Fig. 1b), but the Pd-NCBs shows flake-like structure (Fig. 1c). The TEM images confirm that the Pd-CNSs composed of small clustered nanocrystals with an average particle size (7.85 nm) assembled in 3D porous structure, owing to the direct attachment growth mechanism, while the Pd-NCBs has an obvious uniformly distributed nanocube-like morphology with an average diameter of (9.61 nm) (Figs. 1d and e and S1).

The high-resolution TEM (HRTEM) images disclose the lattice fringes with an interplanar distance of 2.260 Å in Pd-CNSs (Fig. 1f) and 2.262 Å in Pd-NCBs (Fig. 1g), corresponding to {111}facet of face-centred cubic (*fcc*) crystal structure of Pd. The selected area electron diffraction (SAED) patterns denote the usual diffraction rings for {111}, {200}, {220}, {311} and {222} crystal planes of the *fcc* Pd (Figs. 1h and i), as usually observed for Pd-based nanocatalysts [51–53]. Fig. 1j shows the EDX analysis of the Pd-CNSs and Pd-NCBs, which represents the presence of pure Pd atoms with atomic content (100 %), attributable to the complete reduction of Pd^{2+} ions by $NaBH_4$ and L-ascorbic acid. Notably, the estimated Pd mass loading in the aqueous solution was 15.9 mg, whereas the mass of Pd loading in Pd-CNSs was 15.3 mg and 14.31 mg in Pd-NCBs, which indicate the successful reduction of 96 % and 90 % of K_2PdCl_4, using $NaBH_4$ and L-ascorbic acid, respectively. Thus, the mass balance of Pd loading in the powder was 90–96 wt. % of that in aqueous solution.

The XRD analysis of the Pd-CNSs, Pd-NCBs, and Pd/C reveals the diffraction patterns assigned to {111}, {200}, {220}, {311} and {222} crystal planes of *fcc* Pd, in line with the ICDD: 98-006-4920; 98-064-8675; and 98-018-0870, respectively (Fig. 2a) [51,54]. The Pd-CNSs, Pd-NCBs and Pd/C have a similar cubic Fm-3m space group with distinct crystallite sizes of 12.32, 14.38 and 15.02 nm, respectively at {111} facets as calculated from the Scherrer equation. All the catalysts prevalently display high intensity for {111} facet of Pd nanocrystals, which is the most active sites for the electrocatalysis. However, the Pd-CNSs (2.48) has higher ratio of {111}/{200} than Pd-NCBs (2.21) and Pd/C (2.19), which proves that {111} is the most active sites for enhanced EOR activity. There is no resolved peak for Pd–O, due to the complete reduction of Pd^{2+} by $NaBH_4$ and L-ascorbic acid, which implies the uniformity of thus obtained Pd nanocrystals. Notably, compared with spherical-like Pd/C catalyst, the XRD peaks of Pd-CNSs and Pd-NCBs are slightly shifted towards a lower angle value, indicating the lattice expansion with lower lattice parameters of 3.18 Å for Pd-CNSs and 3.20 Å for Pd-NCBs than

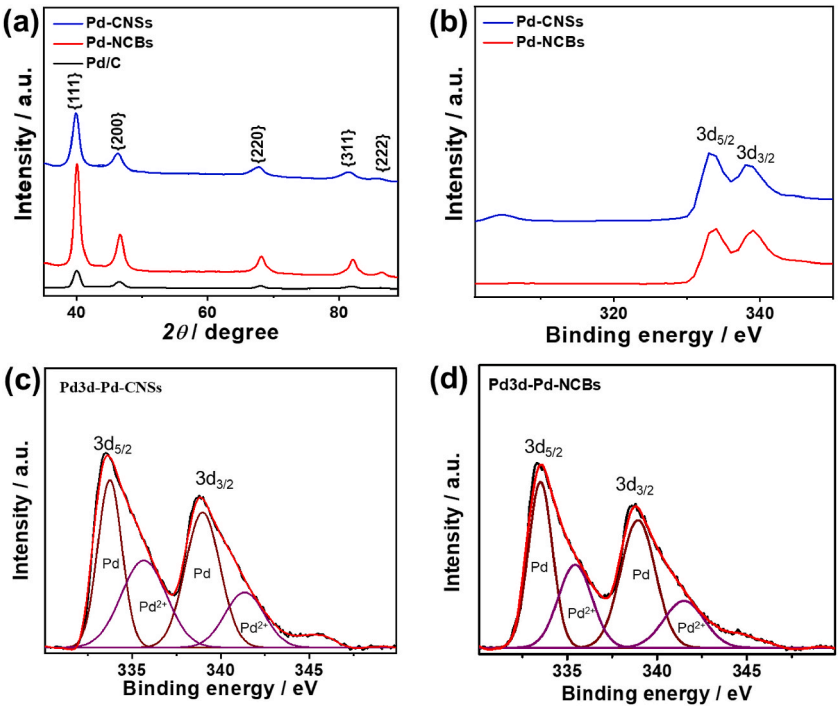

Fig. 2. XRD (a), XPS full survey (b), and high-resolution Pd3d (c, d) of Pd nanocrystals.

that of Pd/C(3.89 Å). This is plausibly owing to the anisotropic clustered nanospheres and nanocubes morphologies with decreased Pd–Pd interatomic distance during the direct attachment growth, which is beneficial in promoting the adsorption/activation of reactants during EOR electrocatalysis.

The XPS full survey shows that Pd is the only element present in the nanocrystals (Fig. 2b). The high-resolution XPS spectra of the Pd3d in Pd-CNSs and Pd-NCBs were fitted into strong peaks assigned to $Pd^{o}3d_{3/2}$ and $Pd^{o}3d_{5/2}$ as the main metallic phase and two weak peaks of $Pd^{2+}3d_{3/2}$ and $Pd^{2+}3d_{5/2}$ as minor oxide phase (Figs. 2c and d**)**. The Pd3d spectra of Pd-CNSs are slightly shifted to lower binding energies compared with those of Pd-NCBs, which implies upshifting of the d-band center of Pd-CNSs than that of Pd-NCBs, clarifying the significant effect of morphology. Upshifting the d-band center of Pd is highly advantageous for promoting the adsorption/activation of reactants and weakening adsorbed intermediates during EOR electrocatalysis. The electrochemical EOR performance and stability of the Pd-CNSs and Pd-NCBs were initially measured in 1.0 M KOH and benchmarked to the commercial Pd/Cs. The cyclic voltammetry (CV) curves of Pd-CNSs, Pd-NCBs, and Pd/C tested in N_2-purged KOH electrolyte display the ideal signatures of Pd-based catalyst with an obvious peak for reduction of PdO at (0.92 V–0.55 V) (Fig. 3a). The ECSA of the Pd-CNSs, Pd-NCBs and Pd/C are about 28.1, 15.2 and 11.2 m^2/g, respectively as calculated from the integration of PdO peak. The higher ECSA of Pd-CNSs than Pd-NCBs and Pd/C is an indication of its inbuilt exposed active centers, meanwhile, the PdO peak of Pd-CNSs and Pd-NCBs are significantly larger and slightly shifted towards lower potential than that of Pd/C catalyst, which implies the ease of oxygenated species formation.

The CV curves measured in 1.0 M KOH/1.0 M ethanol on the tested catalysts reveal distinct oxidation peaks corresponding to the peak current in the anodic direction (I_f) and the peak current in the cathodic direction (I_b), but with a higher I_f on Pd-CNSs (Fig. 3b). The I_f of Pd-CNSs (47.91 mA/cm^2) was nearly 2.4 and 11.4 times greater than those of Pd-NCBs (24.17 mA/cm^2) and Pd/C (4.21 mA/cm^2), correspondingly. The onset potential (E_{onset}) of Pd-CNSs (0.30 V) was lower than those of Pd-NCBs (0.44 V) and Pd/C (0.53 V), implying the quick EOR kinetics on Pd-CNSs as evidenced by the linear sweep voltammetry (LSV) curves (Fig. 3c). This is further corroborated by the high area of forward peak for the Pd-CNSs (2.27 mC cm^{-2}) than Pd-CNBs (1.24 mC cm^{-2}) and Pd/C (1.12 mC cm^{-2}) Figs. S2a-S2c, besides lower E_{Onset}/E_{10} of Pd-CNSs shown with the dash lines on the LSV curves (Fig. S2d). To this end, the Pd-CNSs can generate a higher I_f value under a lower applied potential relative to Pd-NCBs and Pd/C, plausibly attributed to the porous clustered nanospherical morphology, greater ECSA, and ease of formation of Pd–O. This is evident in the superior specific/mass activity of the Pd-CNSs (8.51 mA/cm^2/2.39 A/mg_{Pd}) than those of Pd-NCBs (7.83 mA/cm^2/1.19 A/mg_{Pd}) and Pd/C (1.79 mA/cm^2/0.20 A/mg_{Pd}) at an equivalent Pd mass loading (Fig. 3d). This implies the maximized utilization of Pd active centers in the Pd-CNSs than Pd-NCBs and Pd/C catalysts, owing to the clean surface and porous clustered nanospherical morphology that make Pd active sites more exposed and ease their usage during EOR electrocatalysis. Notably, the EOR specific/mass activities of Pd-CNSs are superior to previously reported Pd catalysts, like Pd-chestnut-bur-like (1.35 mA/cm^2/0.57 A/mg_{Pd}) [36], Pd/CNTs-DPHE-2 nanocrystal (5.27 mA/cm^2/2.12 A/mg_{Pd}) [55], Pd30 multipod (6.56 mA/cm^2/1.42 A/mg_{Pd}) [38], Pd/PPyCC Cauliflower-like (2.04 mA/cm^2/1.19 A/mgPd) [56], Pd nanoclusters (~4.20 mA/cm^2/1.43 A/mg) [57] and others (Table S1).

The Nyquist plots of the Pd-CNSs, Pd-NCBs, and Pd/C were explored to probe the interfacial electrode/electrolyte interaction during EOR in KOH electrolyte (Fig. 3e). All the nanocatalysts display a deformed semi-circle coupled with a diffusion region, but with a smaller diameter of Pd-CNSs than Pd-NCBs and Pd/C, implying its better electrolyte-electrode interaction and charge transfer resistance. This was further fitted by the Voigt electrical equivalent circuit (EEC) to determine the following EIS parameters (Fig. 3e inset): solution resistance (R_s); charge transfer resistance (R_{ct}); constant phase element (CPE); and Warburg impedance (W_d) (Table 1).

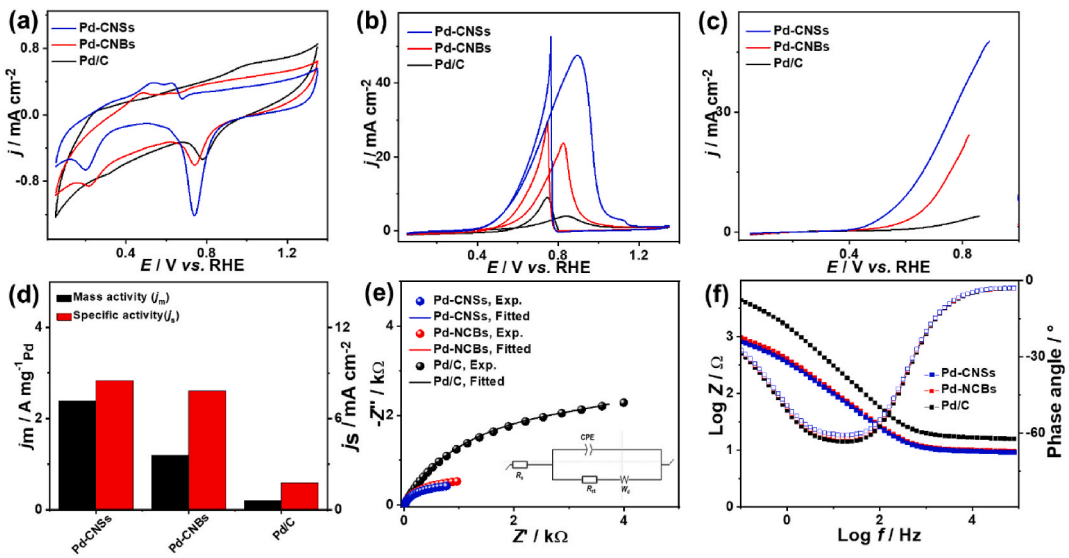

Fig. 3. CVs at 50 mV/s in 1.0 M KOH alone (a), 1.0 M KOH/1.0 M EtOH (b), LSV at 50 mV/s (c), mass/specific activities (d), Nyquist plots with Voigt electrical equivalent circuit (EEC, inset) (e), and Bode plots (f) of Pd nanocrystals and Pd/C.

The lower R_s/R_{ct} of the Pd-CNSs (3.19 Ω/0.85 kΩ) than Pd-NCBs (3.99 Ω/1.06 kΩ) and Pd/C (15.96 Ω/4.24 kΩ) reveal its higher ionic conductivity and lower charge mobility resistance. Following the impedimetric process of the CPE (Z_{CPE}) with accompanying ideality factor (n) in the range of −1 and +1; when $n = 0$, the Z_{CPE} becomes a pure resistor; when $n = 1$, the Z_{CPE} becomes a pure capacitor (i.e., $Z_{CPE} = Z_{Cdl}$); when $n = -1$, the Z_{CPE} becomes pure inductor; and when $n = 0.5$, the Z_{CPE} becomes W_d. The n values in the range 0.5–1.0 are recorded for the electrocatalysts showing their pseudocapacitive behavior during EOR, not an ideal double-double capacitive (C_{dl}). The W_d of 435.86, 532.51 and 674.90 μS $s^{1/2}$ are recorded for Pd-CNSs, Pd-NCBs and Pd/C, respectively. This result elucidates rapid reactants diffusion with a greater diffusion coefficient on the Pd-CNSs than Pd-NCBs and Pd/C. Bode plots further clarify the resistive and capacitive behavior of the nanocatalysts (Fig. 3f). The low overall resistance of the Pd-CNSs in the plots of Log Z (Ω) *vs.* Log f (Hz) at the low-frequency region compared to Pd-CNBs and Pd/C, reveals quick EOR kinetics on Pd-CNSs, while the phase angles (60-65°) plausibly indicate the pseudocapacitive behavior of the nanocatalysts.

Figs. 4a–c show the CV curves of the Pd-CNSs, Pd-NCBs, and Pd/C at scan rates (25–300 mV/s) in 1.0 M KOH/1.0 M EtOH, where increasing scan rates (υ) concurrently increase the I_f values of all the electrocatalysts. Then, plots of I_f *vs.* $\upsilon^{1/2}$ show that all the electrocatalysts possess linearity with the regression coefficients close to unity (i.e., $R^2 = 0.9744$–0.9983) (Fig. 4d). This could serve as evidence for EOR diffusion-controlled process. The high linearity slope of Pd-CNSs (2.14) relative to Pd-NCBs (1.91) and Pd/C (0.60), implies the higher diffusion coefficient of EOR intermediates on the Pd-CNSs compared to Pd-NCBs and Pd/C. The improved alkaline EOR kinetic of the Pd nanocrystals and Pd/C is probed by the Tafel plots that demonstrate a lower Tafel slope ($b = 0.205 \pm 0.012$ V/dec) on the Pd-CNSs than those on Pd-NCBs ($b = 0.250 \pm 0.013$ V/dec) and Pd/C ($b = 0.314 \pm 0.016$ V/dec) (Fig. 4e), confirms the higher EOR kinetics on the Pd-CNSs.

The EOR stability of Pd-CNSs, Pd-NCBs and Pd/C in 1.0 M KOH/1.0 M EtOH was studied with chronoamperometry (CA) for 1600 s at steady-state conditions (Fig. 4f). All the nanocatalysts degrade, but the Pd-CNSs retain a higher current density than Pd-NCBs and Pd/C. The stability of Pd-CNSs, Pd-NCBs and Pd/C toward alkaline EOR was further verified using CV for 1000 cycles (Fig. 5a–c), which displays that the Pd-CNSs retained ~72 % of its initial I_f value compared to Pd-NCBs (~65 %) and Pd/C (~53 %) (Fig. 5d). This is evidenced by the TEM images that reveal no significant morphological changes of the Pd-CNSs and Pd-NCBs after 1000 cycles, while Pd/C showed an obvious aggregation of Pd nanoparticles (Figs. 5e–g).

The FTIR analysis conducted after EOR measurements in alkaline medium shows the vibrational mode of 3350 cm^{-1}, 1720 cm^{-1} and 1470 cm^{-1} attributed to $(OH)_{acid}$, $(C{=}O_{acid})$ and $(C\text{-}O_{acid})$, respectively of acetic acid (CH_3COOH) (Fig. S3). That is the most common product from the EOR on Pd-based catalysts in this study. Thus, the EOR mechanism could be proposed according to the following equations (1)–(4) [18,19,58].

$$\text{Pd-CNSs} + \text{OH-} \rightarrow \text{Pd-CNSs-OH}_{ads} + e^- \quad (1)$$

$$\text{Pd-CNSs} + CH_3CH_2OH \rightarrow \text{Pd-CNSs}(CH_3CH_2OH)_{ads} \quad (2)$$

$$\text{Pd-CNSs}(CH_3CH_2OH)_{ads} + 3OH^- \rightarrow \text{Pd-CNSs}\ (CH_3CO)_{ads} + 3H_2O + 3e^- \quad (3)$$

$$\text{Pd-CNSs}(CH_3CO)_{ads} + \text{Pd-CNSs-OH}_{ads} + OH^- \rightarrow \text{Pd-CNSs} + CH_3COO^- + H_2O \quad (4)$$

The electrochemical CO stripping of the Pd nanocrystals and Pd/C in CO-saturated 1.0 M KOH reveals a peak corresponding to the oxidation of CO, however the oxidation peak diminished after the CO gas was switched to N_2, inferring to the removal of the adsorbed CO on the nanocatalysts (Fig. 6). The CO tolerance of the nanocatalysts was investigated with E_{onset}/oxidation potentials (E_{Oxi}) and oxidation current density (j_{Oxi}). Hence, the Pd-CNSs has relatively lower E_{Onset}/E_{Oxi} (0.57/0.72 V) than Pd-CNBs (0.60/0.76 V) and Pd/C (0.59/0.77 V), which is an indication of facile CO oxidation at lower energy (Figs. 6a–c). This proved that Pd-CNSs has better tolerance toward carbonaceous (CO) species poisoning than Pd-CNBs and Pd/C. Moreover, the Pd-CNSs exhibits superior j_{Oxi} (1.0 mA/cm^2) to Pd-CNBs (0.8 mA/cm^2) and Pd/C (0.60 mA/cm^2), inferring high CO oxidation kinetic on Pd-CNSs. This is attributed to the clustered nanospherical morphology, clean surface, and more expose Pd active sites in the Pd-CNSs.

The EOR of the Pd-CNSs, Pd-NCBs and Pd/C was additionally measured in 0.5 M H_2SO_4 electrolyte. The CV curves of Pd-CNSs, Pd-NCBs and Pd/C measured in N_2-purged H_2SO_4 electrolyte reveal the ideal voltammograms features of Pd, including double-layer hydrogen adsorption/desorption and PdO reduction (Fig. S4a). Notably, the peak assigned to the reduction of Pd–O on the Pd-CNSs is negatively shifted than those of Pd-NCBs and Pd/C, implying its higher active sites and ease of formation of oxygenated species. This is observed in the greater ECSA of Pd-CNSs (11.2 m^2/g) than Pd-NCBs (3.8 m^2/g) and Pd/C (5.1 m^2/g). The CV curves recorded in 0.5 M H_2SO_4/1.0 M EtOH on all catalysts showed EOR features, but with a greater I_f value on the Pd-CNSs (16.12 mA/cm^2) than Pd-NCBs (12.59 mA/cm^2) by 1.3 times and Pd/C (7.07 mA/cm^2) by 2.3 times (Fig. S4b). The LSV show a lower E_{onset} on the Pd-CNSs (0.28 V) than Pd-NCBs (0.54 V) and Pd/C (0.55 V), beside a higher I_f at any potential point (Fig. S4c), implying a better EOR kinetics on the Pd-CNSs. The specific (mass) activity (2.98 mA/cm^2 (0.88 A/mg_{Pd})) of the Pd-CNSs are higher than Pd-CNBs (2.63 mA/cm^2 (0.68 A/mg_{Pd})) and Pd/C (2.09 mA/cm^2 (0.38 A/mg_{Pd})) (Fig. S4d).

Table 1
EIS data of Pd nanocrystals and Pd/C for EOR in 1.0 M KOH/1.0 M EtOH.

	R_s/Ω	R_{ct}/kΩ	CPE/μS.$s^{(1-n)}$	n	W_d/μS.$s^{1/2}$
Pd-CNSs	3.19 ± 0.2	0.85 ± 0.00	80.92 ± 1.32	0.82	435.86 ± 39.87
Pd-NCBs	3.99 ± 0.00	1.06 ± 0.00	110.97 ± 1.58	0.83	532.51 ± 56.24
Pd/C	15.96 ± 0.11	4.24 ± 0.00	120.30 ± 2.20	0.79	674.90 ± 71.06

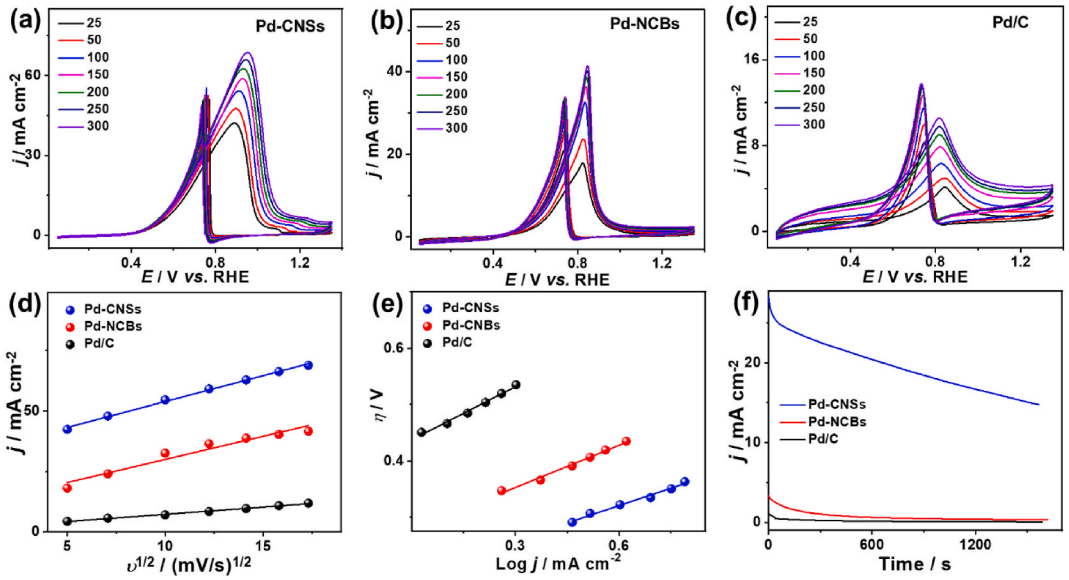

Fig. 4. Scan rate studies (a–c), plots of peaks of forward EtOH oxidation (I_f) vs. square root of scan rates ($\upsilon^{1/2}$) (d), Tafel plots (e), and chronoamperometry (f) of Pd nanocrystals and Pd/C in 1.0 M KOH/1.0 M EtOH.

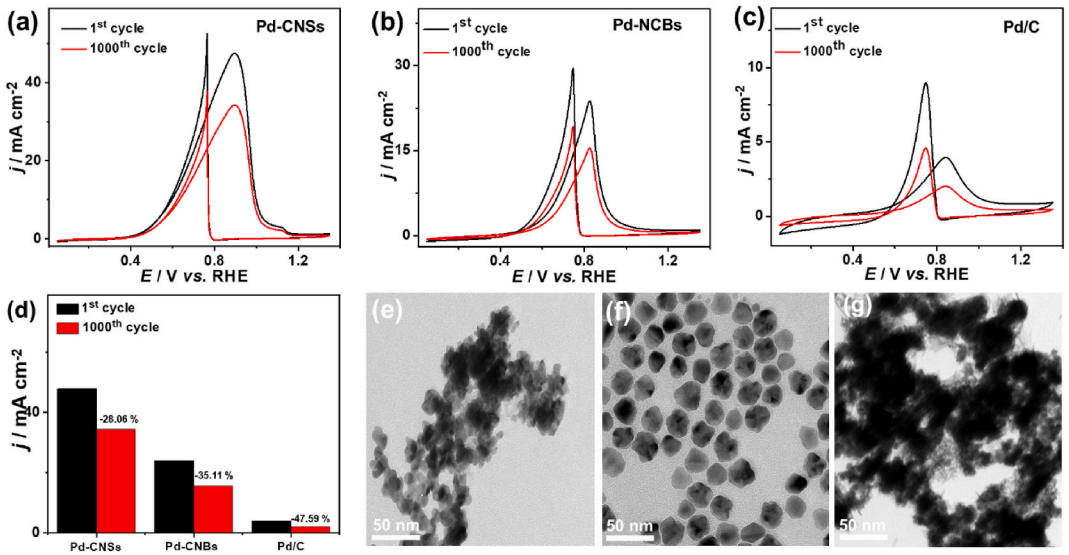

Fig. 5. CV at 50 mV/s for 1st and 1000th cycles (a–c), Bar chart of I_f degradation (d), and TEM images after 1000 cycles of Pd-CNSs (e), Pd-NCBs (f), and Pd/C (g) in 1.0 M KOH/1.0 M EtOH.

The Nyquist plots of Pd-CNSs, Pd-NCBs, and Pd/C show deformed semi-circles, which were fitted with appropriate Voigt EEC to extract the EIS data (Fig. S4e). A similar R_s (~4.50 Ω) is recorded for the Pd-CNSs, Pd-NCBs and Pd/C, which infers the same ionic conductivity of the Pd catalysts in the acidic condition. However, the R_{ct} of the Pd-CNSs (3.47 kΩ) and Pd-NCBs (3.66 kΩ) are lower than that of Pd/C (4.03 kΩ) (Table S2), implying the lowest charge transfer resistance of Pd-CNSs. This is also evident in the lower CPE impedance of the Pd-CNSs and Pd-NCBs than Pd/C, which reveal improved pseudocapacitive properties during EOR electrocatalysis. Meanwhile, the n value of the Pd-CNSs and Pd-NCBs is closer to 0.5, implying their greater intermediates diffusion. The Pd-CNSs has low overall resistance in the plots of Log Z (Ω) *vs.* Log f (Hz) at the low-frequency region relative to Pd-CNBs and Pd/C, indicating high acidic EOR kinetics on Pd-CNSs. The phase angles (64-67°) confirm the pseudocapacitive properties of the nanocatalysts (Fig. S4f).

The CV curves measured at different υ ranged from 25 to 300 mV/s on Pd-CNSs, Pd-CNBs, and Pd/C in 0.5 M H_2SO_4/1.0 M EtOH reveal a linear increase in the I_f values with increasing υ (Figs. S5a-S5c). The plots of I_f *vs.* $\upsilon^{1/2}$ give a linear relationship with the regression coefficients close to 1, revealing that the mechanism of EOR is a diffusion-controlled process (Fig. S5d). The higher slope on Pd-CNSs (0.98) than Pd-NCBs (0.90) and Pd/C (0.50), implies the higher diffusivity of carbonaceous intermediates on Pd-CNSs. This is

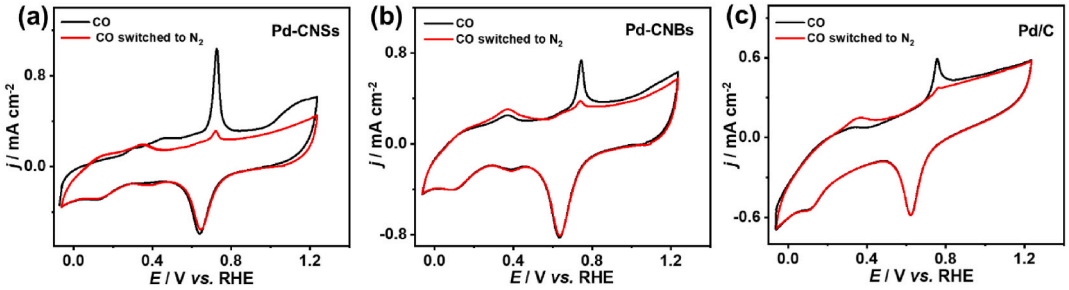

Fig. 6. Electrochemical CO stripping of Pd nanocrystals and Pd/C in CO-saturated 1.0 M KOH at 50 mV/s.

also observed in the Tafel plots showing low b on the Pd-CNSs (0.131 ± 0.010 V/dec) than Pd-NCBs (b = 0.160 ± 0.008 V/dec) and Pd/C (b = 0.167 ± 0.010 V/dec) (Fig. S5e), confirming quicker EOR kinetics on the Pd-CNSs. The CA measured for 1500 s displays a higher stability on the Pd-CNSs than Pd-NCBs and Pd/C (Fig. S5f). Also, after 1000 cycles, the Pd-CNSs preserves ~53 % of its initial I_f value which was more stable than Pd-NCBs (~48 %) and Pd/C (~39 %) (Fig. S6).

The CV curves measured in N_2-purged 0.5 M $NaHCO_3$ electrolyte reveal the voltammogram characteristics of Pd, but with a higher area for hydrogen adsorption/desorption and reduction of PdO on Pd-CNSs than Pd/C and Pd-NCBs (Fig. S7a). The ECSA of Pd-CNSs, Pd/C and Pd-NCBs are about 1.35, 1.30, and 0.80 m^2/g respectively. The CV curves measured in 0.5 M $NaHCO_3$/1.0 M EtOH at 50 mV/s shows the superior EOR activity of the Pd-CNSs with I_f (0.15 mA/cm^2), which is 1.1 times of Pd/C (0.14 mA/cm^2) and 1.5 times of Pd-CNBs (0.10 mA/cm^2) (Fig. S7b). The LSV curves display that the EOR occurs at an earlier E_{onset} (0.35 V) for Pd-CNSs relative to Pd-NCBs (0.54 V) and Pd/C (0.47 V), besides delivering a higher current at a lower applied potential (Fig. S7c). The specific (mass) activity of the Pd-CNSs (0.061 mA/cm^2 (0.0083 A/mg_{Pd})) are substantially greater than those of Pd-CNBs (0.048 mA/cm^2 (0.0054 A/mg_{Pd})) and Pd/C (0.055 mA/cm^2 (0.0078 A/mg_{Pd})) (Fig. S7d). This is of great importance because the self-standing Pd clustered nanospherical structures have enhanced EOR activity than the commercial Pd/Cin all the electrolyte media.

The Nyquist plots of the Pd-CNSs, Pd-NCBs and Pd/C in 0.5 M $NaHCO_3$/1.0 M EtOH reveal semi-circle lines, but with a lower diameter of the Pd-CNSs than Pd/C and Pd-NCBs, implying its lower charge transfer resistance and superior $NaHCO_3$ electrolyte-electrode interaction as further evident in the extracted EIS data using the Voigt EEC (Fig. S7e). All tested nanocatalysts exhibit similar R_s (~42 Ω) inferring their similar ionic conductivity, however, the Pd-CNSs displays a lower R_{ct} and CPE than Pd-CNBs and Pd/C (Table S3), which implies better charge mobility and pseudocapacitive properties of the Pd-CNSs, as also shown in its lower n value that was close to 0.5. This indicates ease of diffusion of EOR intermediates on the Pd-CNSs in the neutral electrolyte.

The Bode plots depict that the Pd-CNSs has a low overall resistance in the plots of Log Z (Ω) *vs.* Log f (Hz) at the low-frequency region relative to Pd-CNBs and Pd/C, implying superior EOR kinetics on the Pd-CNSs. Additionally, the estimated phase angles on the Pd-CNSs, Pd-CNBs and Pd/C are about (52-55°) verifies their pseudocapacitive features (Fig. S7f).

Increasing the υ from 25 to 300 mV/s leads to increasing the EOR current density to reach the highest value at 300 mV/s on the Pd-CNSs, Pd-CNBs and Pd/C in 0.5 M $NaHCO_3$/1.0 M EtOH, but with a superior activity on the Pd-CNSs under all υ (Figs. S8a-S8c). The Randle Sevcik plots (I_f *vs.* $\upsilon^{1/2}$) of the Pd-CNSs, Pd-CNBs and Pd/C give a linear relationship, implying the diffusion-controlled process of the EOR (Fig. S8d). The Pd-CNSs has a higher slope (0.0044) compared to Pd-NCBs (0.0022) and Pd/C (0.0025), implying the better ability of EOR intermediates to diffuse easily on the Pd-CNSs. This is corroborated by the lower Tafel slope on the Pd-CNSs than Pd/C and Pd-CNBs (Fig. S8e). The CA tested for 1500 s demonstrates better stability at steady-state condition with higher current density on the Pd-CNSs than Pd/C and Pd-CNBs (Fig. S8f). This is also observed in the CV curves measured for 1000 cycles, which show that the Pd-CNSs loses only ~30 % of its initial I_f value compared with Pd-NCBs (~40 %) and Pd/C (~48 %) (Fig. S9).

These results clearly warrant the substantial EOR performance of self-standing Pd-CNSs in KOH than in H_2SO_4 and $NaHCO_3$, owing to its clean surface and porous clustered nanospherical structures, which provide abundant active catalytic sites for adsorption of reactants and ease their diffusion to buried atoms. This not only makes the active sites more accessible, but also maximizes their utilization for EOR electrocatalysis. The upshifting d-band center of Pd may enhance the adsorption and activation of ethanol molecules along with facilitating H_2O activation/splitting to generate active OH^- species that subsequently promote the cleavage of C–H cleavage in ethanol and facilitate easy desorption of carbonaceous intermediates. The dissimilar voltammogram features and their related ECSA, mass/specific activity and EIS parameters on the Pd-CNSs, Pd-NCBs, and Pd/C in KOH than those in H_2SO_4 and $NaHCO_3$, infers the significant effect of electrolytes at varied pH and catalyst shapes on the EOR activity and durability. This is due to the following reasons of EOR in alkaline condition: (i) decreased ethanol crossover, i.e., the abundant OH^- species adsorbed on the electrode could facilitate the quick conversion of ethanol to ethanoic acid, (ii) mitigate the danger of adsorbed spectator ions on the electrode that may hinder the electrocatalysis, and (iii) the electrode is less prone to corrosion. However, the results indicate that the porous self-standing 3D clustered spherical nanostructure is the most active and most stable EOR electrocatalyst than the nanocube-like counterpart.

4. Conclusion

This study emphasizes the effect of Pd catalyst shapes and electrolytes at varied pH on the EOR activity and stability. Mainly, porous

Pd clustered nanospheres (Pd-CNSs) and Pd nanocube-like (Pd-NCBs) were synthesized by the chemical reduction of Pd precursor at 0 °C by sodium borohydride ($NaBH_4$) and L-ascorbic acid, respectively. The ice-cooling reduction of $NaBH_4$ induces the burst nucleation and direct attachment growth to generate 3D porous Pd clustered spherical nanostructures, meanwhile, sluggish reduction by L-ascorbic promotes the nucleation and subsequent homogenous growth to form cubic-like nanostructures. To investigate the effect of shapes and electrolytes, the EOR activity and stability of the Pd-CNSs, Pd-NCBs, and Pd/C were measured in alkaline (KOH, pH = 12), acidic (H_2SO_4, pH = 2) and neutral ($NaHCO_3$, pH = 7.4), which displayed the superior performance of the Pd-CNSs than Pd-NCBs, and Pd/C at all the pH values. This originated from the 3D porous clustered nanospherical morphology which provides abundant channels for the adsorption of reactants (CH_3CH_2OH and OH), accelerate their diffusion, makes Pd active centers more accessible, and maximizes their utilization during EOR electrocatalysis. The electrolyte-electrode interaction and electron mobility in KOH were better than in H_2SO_4 and $NaHCO_3$ on the as-synthesize nanocatalysts. Notably, the EOR specific/mass activities of the Pd-CNSs reached (8.51 mA/cm^2/2.39 A/mg_{Pd}) in KOH, (2.98 mA/cm^2/0.88 A/mg_{Pd}) in H_2SO_4, and (0.061 mA/cm^2/0.0083 A/mg_{Pd}) in $NaHCO_3$, in addition to its great stability after 1000 cycles, implies better activity in KOH electrolyte. The study herein verifies that porous self-standing 3D Pd clustered spherical nanostructures are preferred for the EOR than non-porous 0D special-like supported Pd/C and multi-dimensional self-standing cube-like Pd nanostructures over a wide pH values.

Author contribution statement

Adewale K. Ipadeola: Conceived and designed the experiments; Performed the experiments; Analyzed and interpreted the data; Wrote the paper.

Belal Salah: Performed the experiments; Analyzed and interpreted the data.

Alaa Ghanem, Doniyorbek Ahmadaliev, Mohammed A. Sharaf: Analyzed and interpreted the data; Wrote the paper.

Aboubakr M. Abdullah: Contributed reagents, materials analysis tools or data.

Kamel Eid: Conceived and designed the experiments; Wrote the paper.

Data availability

Data will be made available on request.

Declaration of competing interest

The authors declare that they have no known competing financial interests or personal relationships that could have appeared to influence the work reported in this paper.

Acknowledgements

This work was supported by the Qatar University High Impact Internal Grant (QUHI-CAM-22/23-550) and Qatar National Research Fund (NPRP13S-0117-200095). The statements made herein are solely the responsibility of the authors. The authors are grateful to the Environmental Science Center (ESC), Qatar University, for the ICP-OES analysis.

Appendix B. Supplementary data

Supplementary data related to this article can be found at https://doi.org/10.1016/j.heliyon.2023.e16890.

References

[1] Q. Lu, J. Li, K. Eid, X. Gu, Z. Wan, W. Li, R.S. Al-Hajri, A.M. Abdullah, Facile one-step aqueous-phase synthesis of porous PtBi nanosponges for efficient electrochemical methanol oxidation with a high CO tolerance, J. Electroanal. Chem. 916 (2022), 116361.

[2] K. Eid, Y.H. Ahmad, S.Y. AlQaradawi, N.K. Allam, Rational design of porous binary Pt-based nanodendrites as efficient catalysts for direct glucose fuel cells over a wide pH range, Catal. Sci. Technol. 7 (2017) 2819–2827.

[3] M.A. Ahsan, T. He, K. Eid, A.M. Abdullah, M.F. Sanad, A. Aldalbahi, B. Alvarado-Tenorio, A. Du, A.R. Puente Santiago, J.C. Noveron, Controlling the interfacial charge polarization of MOF-derived 0D–2D vdW architectures as a unique strategy for bifunctional oxygen electrocatalysis, Appl. Mater. Interfaces 14 (2022) 3919–3929.

[4] H. Mohammadian-Sarcheshmeh, M. Mazloum-Ardakani, Recent advancements in compact layer development for perovskite solar cells, Heliyon 4 (2018), e00912.

[5] H.I. Abdu, K. Eid, A.M. Abdullah, M.H. Sliem, A. Elzatahry, X. Lu, Dry ice-mediated rational synthesis of edge-carboxylated crumpled graphene nanosheets for selective and prompt hydrolysis of cellulose and eucalyptus lignocellulose under ambient reaction conditions, Green Chem. 22 (2020) 5437–5446.

[6] Q. Lu, A. Abdelgawad, J. Li, K. Eid, Non-Metal-Doped porous carbon nitride nanostructures for photocatalytic green hydrogen production, Int. J. Mol. Sci. 23 (2022), 15129.

[7] A. Gamal, K. Eid, A.M. Abdullah, Engineering of Pt-based nanostructures for efficient dry (CO2) reforming: strategy and mechanism for rich-hydrogen production, Int. J. Hydrogen Energy 47 (2021) 5901–5928.

[8] R. Singh, A. Altaee, S. Gautam, Nanomaterials in the advancement of hydrogen energy storage, Heliyon 6 (2020), e04487.

[9] A.K. Ipadeola, N.Z. Lisa Mathebula, M.V. Pagliaro, H.A. Miller, F. Vizza, V. Davies, Q. Jia, F. Marken, K.I. Ozoemena, Unmasking the latent passivating roles of Ni (OH) 2 on the performance of Pd–Ni electrocatalysts for alkaline ethanol fuel cells, ACS Appl. Energy Mater. 3 (2020) 8786–8802.

[10] F. Wu, K. Eid, A.M. Abdullah, W. Niu, C. Wang, Y. Lan, A.A. Elzatahry, G. Xu, Unveiling one-pot template-free fabrication of exquisite multidimensional PtNi multicube nanoarchitectonics for the efficient electrochemical oxidation of ethanol and methanol with a great tolerance for CO, Appl. Mater. Interfaces 12 (2020) 31309–31318.
[11] C.V. Almeida, G. Tremiliosi-Filho, K.I. Eguiluz, G.R. Salazar-Banda, Improved ethanol electro-oxidation at Ni@ Pd/C and Ni@ PdRh/C core–shell catalysts, J. Catal. 391 (2020) 175–189.
[12] R. Rizo, A. Bergmann, J. Timoshenko, F. Scholten, C. Rettenmaier, H.S. Jeon, Y.-T. Chen, A. Yoon, A. Bagger, J. Rossmeisl, B. Roldan Cuenya, Pt-Sn-Co nanocubes as highly active catalysts for ethanol electro-oxidation, J. Catal. 393 (2021) 247–258.
[13] G. Zhang, Y. Wang, Y. Ma, Y. Zheng, H. Zhang, M. Tang, Y. Dai, Ultrathin samarium-doped palladium nanocrystals with exotic shapes for efficient electrocatalytic ethanol oxidation, Catal. Today 409 (2023) 63–70.
[14] U. Banin, N. Waiskopf, L. Hammarström, G. Boschloo, M. Freitag, E.M. Johansson, J. Sá, H. Tian, M. Johnston, L. Herz, Nanotechnology for catalysis and solar energy conversion, Nanotechnology 32 (2020), 042003.
[15] A.K. Ipadeola, K. Eid, A.K. Lebechi, A.M. Abdullah, K.I. Ozoemena, Porous multi-metallic Pt-based nanostructures as efficient electrocatalysts for ethanol oxidation: strategy and mechanism, Electrochem. Commun. 140 (2022), 107330.
[16] A. Santasalo-Aarnio, E. Sairanen, R.M. Arán-Ais, M.C. Figueiredo, J. Hua, J.M. Feliu, J. Lehtonen, R. Karinen, T. Kallio, The activity of ALD-prepared PtCo catalysts for ethanol oxidation in alkaline media, J. Catal. 309 (2014) 38–48.
[17] A. Velázquez-Palenzuela, E. Brillas, C. Arias, F. Centellas, J.A. Garrido, R.M. Rodríguez, P.-L. Cabot, Structural analysis of carbon-supported Ru-decorated Pt nanoparticles synthesized using forced deposition and catalytic performance toward CO, methanol, and ethanol electro-oxidation, J. Catal. 298 (2013) 112–121.
[18] A.K. Ipadeola, R. Barik, S.C. Ray, K.I. Ozoemena, Bimetallic Pd/SnO2 nanoparticles on metal organic framework (MOF)-derived carbon as electrocatalysts for ethanol oxidation, Electrocatalysis 10 (2019) 366–380.
[19] K.I. Ozoemena, Nanostructured platinum-free electrocatalysts in alkaline direct alcohol fuel cells: catalyst design, principles and applications, RSC Adv. 6 (2016) 89523–89550.
[20] G.M. Alvarenga, I.B. Coutinho Gallo, H.M. Villullas, Enhancement of ethanol oxidation on Pd nanoparticles supported on carbon-antimony tin oxide hybrids unveils the relevance of electronic effects, J. Catal. 348 (2017) 1–8.
[21] D.D. Hibbitts, M. Neurock, Influence of oxygen and pH on the selective oxidation of ethanol on Pd catalysts, J. Catal. 299 (2013) 261–271.
[22] H. Yang, Z. Yu, S. Li, Q. Zhang, J. Jin, J. Ma, Ultrafine palladium-gold-phosphorus ternary alloyed nanoparticles anchored on ionic liquids-noncovalently functionalized carbon nanotubes with excellent electrocatalytic property for ethanol oxidation reaction in alkaline media, J. Catal. 353 (2017) 256–264.
[23] Q. Chen, H. Jin, T. Cheng, Z. Wang, Y. Ren, J. Tian, Y. Zhu, Small amount of main group metal atoms matters: ultrathin Pd-based alloy nanowires enabling high activity and stability towards efficient oxygen reduction reaction and ethanol oxidation, Nanoscale 15 (2023) 3772–3779.
[24] A. Elsheikh, J. Torrero, S. Rojas, J. McGregor, In-situ FTIR spectroscopy investigation of carbon-supported PdAuNi electrocatalysts for ethanol oxidation, J. Electroanal. Chem. 928 (2023), 116985.
[25] K. Eid, Y.H. Ahmad, H. Yu, Y. Li, X. Li, S.Y. AlQaradawi, H. Wang, L. Wang, Rational one-step synthesis of porous PtPdRu nanodendrites for ethanol oxidation reaction with a superior tolerance for CO-poisoning, Nanoscale 9 (2017) 18881–18889.
[26] C. Zhai, J. Hu, M. Zhu, Three dimensional PdAg nanoflowers as excellent electrocatalysts towards ethylene glycol oxidation, J. Electroanal. Chem. 806 (2017) 1–7.
[27] W. Zhu, L. Zhang, P. Yang, X. Chang, H. Dong, A. Li, C. Hu, Z. Huang, Z.J. Zhao, J. Gong, Morphological and compositional design of Pd–Cu bimetallic nanocatalysts with controllable product selectivity toward CO2 electroreduction, Small 14 (2018), 1703314.
[28] Q. Yun, Q. Lu, C. Li, B. Chen, Q. Zhang, Q. He, Z. Hu, Z. Zhang, Y. Ge, N. Yang, Synthesis of PdM (M= Zn, Cd, ZnCd) nanosheets with an unconventional face-centered tetragonal phase as highly efficient electrocatalysts for ethanol oxidation, ACS Nano 13 (2019) 14329–14336.
[29] S. Li, J. Shu, S. Ma, H. Yang, J. Jin, X. Zhang, R. Jin, Engineering three-dimensional nitrogen-doped carbon black embedding nitrogen-doped graphene anchoring ultrafine surface-clean Pd nanoparticles as efficient ethanol oxidation electrocatalyst, Appl. Catal. B Environ. 280 (2021), 119464.
[30] C. Liu, T. Wu, F. Zeng, X. Pan, G. Li, K. Teng, X. Ran, Q. Qu, L. Li, L. Yang, High-selective and effective carbon nanotubes supported ultrasmall PtPdRh electrocatalysts for ethanol oxidation, Electrochim. Acta 437 (2023), 141531.
[31] Liu C., Ran X., Li G., Li Z., Du G., Yang L., Li L., Qu Q., Facile-synthesis and shape-adjustment of irregular gravel-like PtPd nanocatalysts by three-dimensional hyperbranched polyamide (HBPA) with enhanced activity in ethanol oxidation, Int. J. Hydrogen Energy (2023) (in press) doi.org/10.1016/j.ijhydene.2023.03.054.
[32] C. Karaman, Engineering of N,P,S-Triple doped 3-dimensional graphene architecture: catalyst-support for "surface-clean" Pd nanoparticles to boost the electrocatalysis of ethanol oxidation reaction, Int. J. Hydrogen Energy 48 (2023) 6691–6701.
[33] Q. Shen, Q. Min, J. Shi, L. Jiang, J.-R. Zhang, W. Hou, J.-J. Zhu, Morphology-controlled synthesis of palladium nanostructures by sonoelectrochemical method and their application in direct alcohol oxidation, J. Phys. Chem. C 113 (2009) 1267–1273.
[34] K. Qi, Q. Wang, W. Zheng, W. Zhang, X. Cui, Porous single-crystalline palladium nanoflowers with enriched {100} facets for highly enhanced ethanol oxidation, Nanoscale 6 (2014) 15090–15097.
[35] Y. Zhang, X. Zhu, J. Guo, X. Huang, Controlling palladium nanocrystals by solvent-induced strategy for efficient multiple liquid fuels electrooxidation, Appl. Mater. Interfaces 8 (2016) 20642–20649.
[36] S.J. Ye, S.W. Kang, K.W. Choi, S.W. Han, O.O. Park, Synthesis of chestnut-bur-like palladium nanostructures and their enhanced electrocatalytic activities for ethanol oxidation, Nanoscale 6 (2014) 4182–4187.
[37] C. Shang, W. Hong, Y. Guo, J. Wang, E. Wang, Water-based synthesis of palladium trigonal bipyramidal/tetrahedral nanocrystals with enhanced electrocatalytic oxidation activity, Chem.–Eur. J. 23 (2017) 5799–5803.
[38] S. Lee, H. Cho, H.J. Kim, J.W. Hong, Y.W. Lee, Shape-and size-controlled palladium nanocrystals and their electrocatalytic properties in the oxidation of ethanol, Materials 14 (2021) 2970.
[39] D. Yang, J. Carpena-Núnez, L.F. Fonseca, A. Biaggi-Labiosa, G.W. Hunter, Shape-controlled synthesis of palladium and copper superlattice nanowires for high-stability hydrogen sensors, Sci. Rep. 4 (2014) 1–6.
[40] H. Dong, Y.-C. Chen, C. Feldmann, Polyol synthesis of nanoparticles: status and options regarding metals, oxides, chalcogenides, and non-metal elements, Green Chem. 17 (2015) 4107–4132.
[41] Z. Zhang, T. Sun, C. Chen, F. Xiao, Z. Gong, S. Wang, Bifunctional nanocatalyst based on three-dimensional carbon nanotube–graphene hydrogel supported Pd nanoparticles: one-pot synthesis and its catalytic properties, Appl. Mater. Interfaces 6 (2014) 21035–21040.
[42] H. Lei, X. Li, C. Sun, J. Zeng, S.S. Siwal, Q. Zhang, Galvanic replacement–mediated synthesis of Ni-supported Pd nanoparticles with strong metal–support interaction for methanol electro-oxidation, Small 15 (2019), 1804722.
[43] M. Mehrabi, P. Parvin, A. Reyhani, S. Mortazavi, Hybrid laser ablation and chemical reduction to synthesize Ni/Pd nanoparticles decorated multi-wall carbon nanotubes for effective enhancement of hydrogen storage, Int. J. Hydrogen Energy 43 (2018) 12211–12221.
[44] H. Huang, L. Zhang, T. Lv, A. Ruditskiy, J. Liu, Z. Ye, Y. Xia, Five-Fold twinned Pd nanorods and their use as templates for the synthesis of bimetallic or hollow nanostructures, ChemNanoMat 1 (2015) 246–252.
[45] F. Kettemann, M. Wuithschick, G. Caputo, R. Kraehnert, N. Pinna, K. Rademann, J. Polte, Reliable palladium nanoparticle syntheses in aqueous solution: the importance of understanding precursor chemistry and growth mechanism, CrystEngComm 17 (2015) 1865–1870.
[46] M.H. Hussain, N.F. Abu Bakar, A.N. Mustapa, K.-F. Low, N.H. Othman, F. Adam, Synthesis of various size gold nanoparticles by chemical reduction method with different solvent polarity, Nanoscale Res. Lett. 15 (2020) 1–10.
[47] B. Lim, M. Jiang, P.H. Camargo, E.C. Cho, J. Tao, X. Lu, Y. Zhu, Y. Xia, Pd-Pt bimetallic nanodendrites with high activity for oxygen reduction, Science 324 (2009) 1302–1305.
[48] Y. Wang, H.-C. Peng, J. Liu, C.Z. Huang, Y. Xia, Use of reduction rate as a quantitative knob for controlling the twin structure and shape of palladium nanocrystals, Nano Lett. 15 (2015) 1445–1450.

[49] F.J. Vidal-Iglesias, R.M. Aran-Ais, J. Solla-Gullon, E. Garnier, E. Herrero, A. Aldaz, J.M. Feliu, Shape-dependent electrocatalysis: formic acid electrooxidation on cubic Pd nanoparticles, Phys. Chem. Chem. Phys. 14 (2012) 10258–10265.
[50] M. Jin, H. Zhang, Z. Xie, Y. Xia, Palladium nanocrystals enclosed by {100} and {111} facets in controlled proportions and their catalytic activities for formic acid oxidation, Energy Environ. Sci. 5 (2012) 6352–6357.
[51] B. Salah, K. Eid, A.M. Abdelgwad, Y. Ibrahim, A.M. Abdullah, M.K. Hassan, K.I. Ozoemena, Titanium carbide (Ti3C2Tx) MXene ornamented with palladium nanoparticles for electrochemical CO oxidation, Electroanalysis 34 (2022) 677–683.
[52] S. Navaladian, B. Viswanathan, T. Varadarajan, R. Viswanath, A rapid synthesis of oriented palladium nanoparticles by UV irradiation, Nanoscale Res. Lett. 4 (2009) 181–186.
[53] B. Suresh Kumar, A.J. Amali, K. Pitchumani, Fabrication of Pd nanoparticles embedded C@ Fe3O4 core–shell hybrid nanospheres: an efficient catalyst for cyanation in aryl halides, Appl. Mater. Interfaces 7 (2015) 22907–22917.
[54] C. Li, K. Eid, H. Wang, Y. Deng, S. Lu, X. Li, L. Wang, H. Gu, One-pot synthesis of bimetallic PdCu nanoframes as an efficient catalyst for the methanol oxidation reaction, New J. Chem. 42 (2018) 798–801.
[55] S. Li, M. Yang, R. Jin, H. Niu, C. Liao, H. Yang, J. Jin, J. Ma, Coupling palladium nanocrystals over D-phenylalanine-functionalized carbon nanotubes as an advanced electrocatalyst for hydrogen evolution and ethanol oxidation, Electrochim. Acta 364 (2020), 137290.
[56] H. Han, Y. Noh, Y. Kim, V. Yadav, S. Park, W. Yoon, S. Lee, W.B. Kim, Electrocatalytic oxidations of formic acid and ethanol over Pd catalysts supported on a doped polypyrrole-carbon composite, ChemistrySelect 2 (2017) 6260–6268.
[57] R. Ding, X. Wu, G. Han, Q. Wang, H. Lu, H. Li, A. Fu, P. Guo, Synthesis of palladium colloidal nanocrystal clusters and their enhanced electrocatalytic properties, ChemElectroChem 2 (2015) 427–433.
[58] R. Jiang, D.T. Tran, J.P. McClure, D. Chu, A class of (Pd–Ni–P) electrocatalysts for the ethanol oxidation reaction in alkaline media, ACS Catal. 4 (2014) 2577–2586.